The Role of Microstructural Evolution on the Fatigue Behavior of Additively Manufactured Ti-6Al-4V Alloy

Bryan Naab [1, 2*], Mert Celikin [1, 2]

[1] Materials Design and Processing Laboratory, School of Mechanical and Materials Engineering, University College Dublin, Ireland

[2] SFI I-Form Advanced Manufacturing Research Centre, Ireland

* bryan.naab@ucdconnect.ie

Abstract

The fatigue behavior of additively manufactured Ti-6Al-4V via Laser Powder Bed Fusion (L-PBF) was evaluated in three different conditions, as-built, heat-treated and hot isostatically pressed (HIP'ed). Fractography analysis interpreted together with the *S-N* curves indicates that fatigue failure in as-built and heat-treated conditions where <0.2% porosity was present, was mainly driven by early-stage crack growth. However, crack initiation was determined to be the main controlling factor for fatigue deformation of HIP'ed samples. Moreover, a strong correlation between the impact energy and fatigue limit was found. The findings were based on detailed microstructural and crystallographic characterization, as well as mechanical testing. The as-built and heat-treated conditions exhibited poor fatigue response in comparison to HIP'ed which is largely attributed to the lower levels of porosity identified. Even though similar levels of porosity are present in as-built and heat-treated samples, improvement in fatigue limit was determined in the heat-treated condition due to phase transformation and microstructural coarsening leading to reduction in micro-strain.

Keywords: Additive Manufacturing, Selective Laser Melting (SLM), fatigue behaviour, Titanium alloys, microstructural characterization

Introduction

Additively manufactured (AM) Ti-6Al-4V (Ti64) alloy has already started to be used commercially by the biomedical and aerospace industries for producing critical titanium (Ti) based components, such as orthopedic implants, structural brackets, or fuel injection systems. The laser powder bed fusion (L-PBF) AM process is widely used in industry due to its ability to produce parts with complex geometry in a single step and with good dimensional accuracy [1]. However, L-PBF AM Ti64-components demonstrate lower fatigue limits when compared to conventionally produced wrought Ti64 [2, 3]. Process induced internal and surface defects have been reported to be the main cause for the limited fatigue life of L-PBF AM-Ti64 [4–10]. Consistently, the increase in the fatigue life of AM-Ti64 alloy upon hot isostatic pressing (HIP) treatment, which decreases the porosity levels below 0.015% in volume [11, 12], is well-known and applied in both biomedical and aerospace industries regularly [13, 14]. The fact that AM-Ti64 components are still reported to possess inferior fatigue resistance than wrought Ti64 [15], raises concerns for widening the use of AM technology in processing fatigue critical components. Unambiguous understanding of the role of microstructural evolution on fatigue behaviour is critical for the applicability of AM for parts prone to fatigue failure.

The possible formation of structural defects such as pores in Ti64 alloy during L-PBF remains a risk even after the optimization of AM processing parameters including laser power, hatch spacing, laser scan speed etc. [11, 16]. Process related pores have been shown to negatively affect the fatigue properties of Ti64 manufactured via L-PBF and Electron Beam Melting (EBM) [10, 17]. Pore morphology, orientation and shape are directly linked to the scan strategy and processing parameters used in AM, for example the lack of laser power has been identified as the reason for lack of fusion porosity formation in L-PBF [18]. The presence of pores decreases the ductility and increases the possibility of brittle failure in tensile testing [11, 18, 19]. During fatigue failures, it has been shown that cracks frequently originate at pores associated with non-melted powder particles [17] and high porosity levels with close proximity to the surface are more detrimental to fatigue strength due to the increased localized stress intensity. Moreover, the presence of porosity also influences the crack propagation path [18]; cracks grow preferentially through pores rather than through the bulk material. Hence cracks may adjust their growth path according to the porosity distribution. The pore size $\sqrt{A}$, the applied fatigue stress and the number of fatigue cycles endured N_f, are linked [10, 17]; increased $\sqrt{A}$ leads to a reduced fatigue resistance. For example, Tammas-Williams et al. [10] estimated the relationship between $\sqrt{A}$ and N_f for EBM Ti64 stressed at 600 MPa to be described by equation 1.

$$\sqrt{A} = 10^{5.1(\pm 0.2)} {N_f}^{-0.67(\pm 0.04)} \qquad \textit{Equation 1}$$

Where A is the pore area in the plane perpendicular to the loading direction, N_f is the number of fatigue cycles to failure. The application of costly HIP cycles which involves the use of high pressures and temperatures, typically 100 MPa at 850 °C, to reduce the porosity content in AM-Ti64, increases the fatigue limit considerably. Typical fatigue limits reported for L-PBF – as-built, L-PBF – HIP and wrought Ti64 are summarised in Table 1. Fatigue strength as low as 350 MPa are reported for L-PBF – as-built, with HIP treatments achieving fatigue strengths of up to 620 MPa. Wrought Ti64 is reported to have a fatigue limit of 630 – 680 MPa.

Table 1: Reported fatigue strength of Ti64

Processing condition	Fatigue strength (MPa)	Reported literature
L-PBF – as-built (machined)	350 – 550	[4, 15, 20, 21]
L-PBF – HIP (machined)	560 – 620	[4, 15, 22]
Wrought (machined)	630 – 710	[15, 23, 24]

Understanding the lower fatigue limits upon HIP treatment in AM Ti64 in comparison to wrought Ti64 is critical for widening the use of AM. HIP treatments may not only decrease the porosity levels but also coarsen the microstructural features such as the α-lath size and minimize the residual stresses. In High Cycle Fatigue (HCF) of a conventional wrought Ti64, it was reported that both the α-lath width and the grain size are directly linked with the fatigue limit. Finer grains and smaller α-lath spacing result in higher fatigue strength in HCF regime [25]. Moreover, finer equiaxed grains in comparison to coarser lamella are stated to be more resistant to fatigue crack initiation but facilitates crack propagation. Even though the effect of microstructural influence on fatigue resistance has been understood for conventional processing of Ti64, not many studies have focused on the role of microstructure on fatigue of AM-Ti64.

Another critical factor influencing fatigue behaviour is the surface finish of metals. The surface roughness is mainly controlled by machining or electropolishing for most fatigue critical applications. Ti64 produced by EBM and direct metal laser sintering (DMLS) with an as-built surface roughness, with average RS_m values of 696 and 535 µm, respectively, showed a 3-fold increase in the fatigue strength when polished to a fine surface finish[26]. When the surface roughnesses of specimens in the as-built condition were benchmarked against HIP'ed specimens with similar surface roughnesses, there was only a very slight improvement in the fatigue strength upon HIP [26]. This indicates the surface roughness of as-built AM Ti64 overshadows the influence of porosity level on the fatigue response.

L-PBF produces very fine, non-homogenous, thermally unstable lamellar microstructures [27] as well as high levels of residual stress in Ti64 alloy [28]. Resulting from steep heating (~10^6 - 10^7 ˚C

/sec) and rapid cooling (10^3 ˚C /sec) during the L-PBF process, columnar prior *β* grains transform to martensitic-*α'* phase instead of equilibrium *α* and *β* structure. An increase in the fatigue crack growth threshold stress intensity factor (ΔK_{th}) was reported when comparing the as-built state to stress relieved L-PBF Ti64. Stress relieving heat treatment (800 °C for 2 hours) did not significantly alter the microstructure but did increase the ΔK_{th} from 1.4 to 4 MPa$\sqrt{m}$ indicating that stress relief of as-built samples can prevent the growth of early stage fatigue cracks [22]. Wycisk found fatigue crack initiation to be the main controlling factor in determining the fatigue life in L-PBF Ti64 which was attributed to the microstructure [29].

Our objective in this investigation is to understand the role of microstructural evolution on the fatigue behavior of L-PBF AM Ti64 upon post-processing heat treatment or HIP. This is achieved via in-depth mechanical (fatigue, tensile and Charpy impact tests) and structural characterization (X-ray computed tomography-CT, x-ray diffraction-XRD, OM, SEM/EDS) of L-PBF AM-Ti64 alloys in as-built, heat-treated and HIP'ed conditions.

1. Materials and methods

1.1. Raw materials

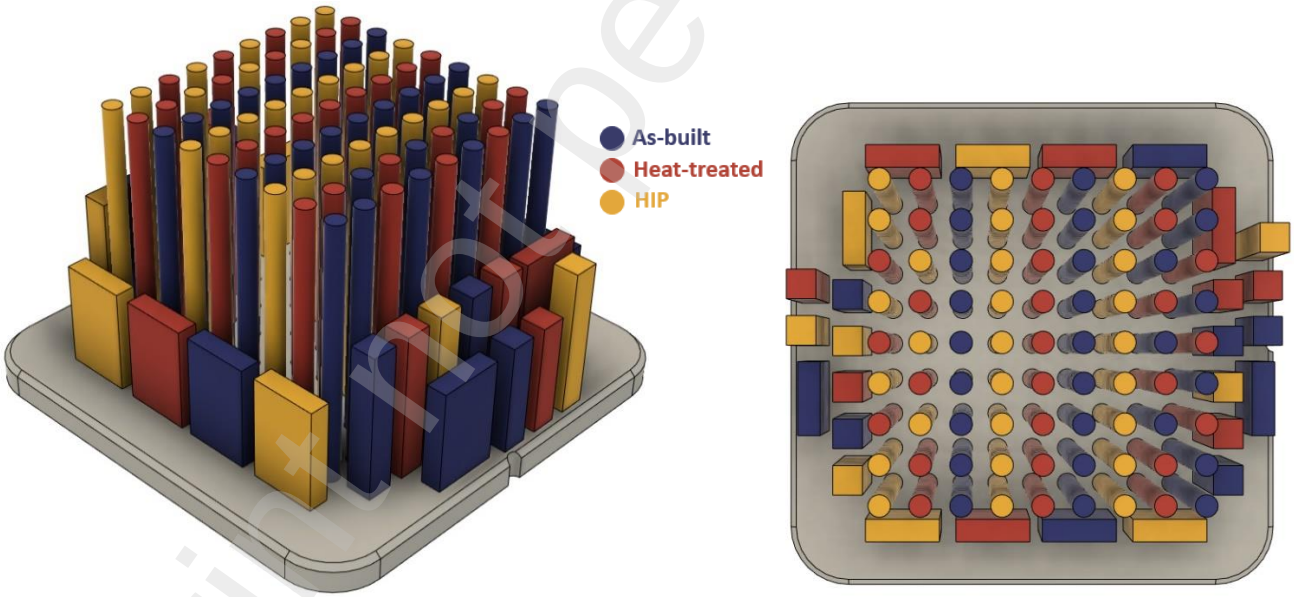

Figure 1: SLM Build layout. (left) Side view, (right).

The build layout used to prepare samples for this study is shown in Figure 1. Net shape mechanical specimens and samples for materials characterization were additively manufactured via L-PBF using raw Ti64 (grade 23 ELI) powder, with particle size D_{50}: 30 – 36 µm. Manufacturing was conducted using a production scale powder bed system, Renishaw RenAM 500M with a 1070 nm wavelength, 500 W, pulsed Yb:YAG (λ = 1.07 µm) laser. Chemical compositions of the powder and as-built Ti64 are given in Table 3. Powder composition was provided by the supplier of the powder and represents the virgin state. The as-built chemical composition was analyzed using Inductively

Coupled Plasma, Carbon Analysis and Inert Gas Fusion. The powder was within spec for Ti-6Al-4V grade 23 at the time of purchase, however the as-built material oxygen content exceeds the 0.13% limit for O_2.

Table 2: Chemical analysis

Element	Al	C	Fe	H_2	N_2	O_2	Ti	V	Y
As-built	6.31	0.018	0.18	0.0058	0.023	0.16	Bal	3.96	<0.005
Powder	6.34	0.03	0.19	0.002	<0.01	0.13	Bal	3.81	<0.001

1.2. Material processing

Heat treatments were performed to achieve a dissimilar microstructure to the as-built state, the heat treatment was developed based on work by G. T. Haar et al. [30], D. Wang et al. [31] and B. Vrancken et al. [32]. Heat treatment was conducted in a Nabertherm heat treatment furnace, under argon (Ar) atmosphere with 99.98% purity. Temperature was raised from room temperature (RT) to 850°C with a heating rate of 5°C/min, followed by an isothermal hold for two (2) hours. Samples were then furnace cooled at 5°C/min to 450°C and subsequently air quenched, back to RT. HIP treatment was conducted by Stryker using their proprietary process.

1.3. Materials Characterization

Specimens for microstructural analysis were prepared by cutting 10 mm sections parallel to the build direction, at a build height of approximately 60 mm, using a Buehler precision saw and silicon carbide cut-off wheel. Specimens were ground using 220 grit sandpaper, polished using a 9 µm diamond suspension, followed by a final polishing step using a 70% 0.04 µm silica suspension and 30% (30% diluted) H_2O_2. Etching was performed using Krolls' reagent (2% HF, 6% HNO_3 and 92% DI) for a duration of 15 seconds.

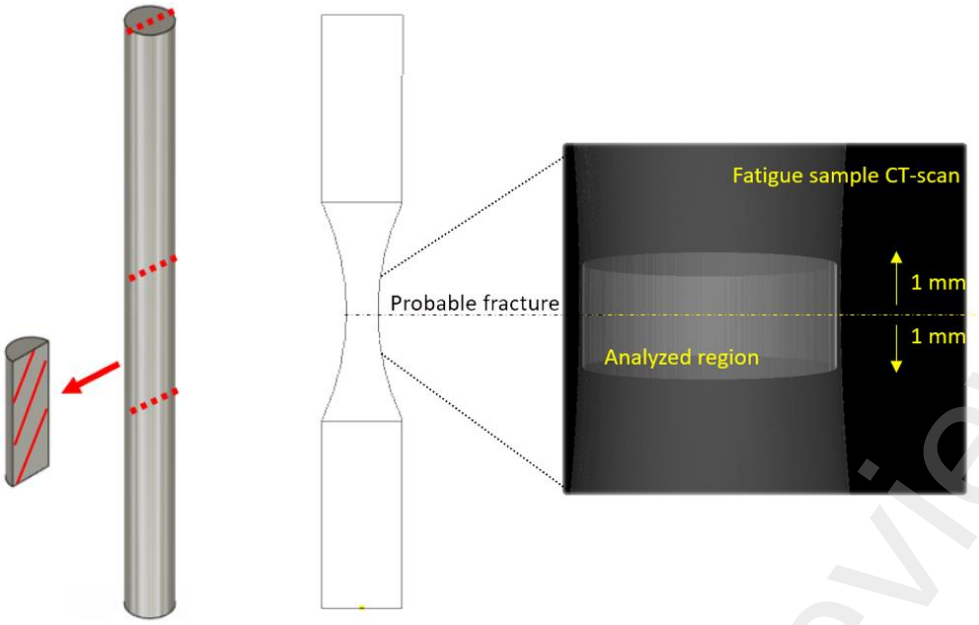

Figure 2: Diagram showing where microstructural analysis was conducted, imaged region marked in red (left). Diagram showing microCT scanned region on sample (right).

XRD analysis was conducted on the same samples using a Siemens D500 X-ray diffractometer, with Cu-K_α source with a wavelength (λ) of 1.5406 Å. The diffractometer was set to scan the 2θ range of 30° – 80°, with a step increment of 0.02° and a holding time of 4 seconds, a custom MATLAB script was developed to determine the peak position and full width half maximum (FWHM). The microstrain was computed using the Williamson-Hall method [33]. Micro-CT scanning was conducted on the gauge section of machined fatigue specimens using a "Phoenix Nanotom® M" micro-CT and nano-CT computed tomography system at UCD. In Figure 2, the region that was scanned by microCT is highlighted.

Fracture surface analysis was performed using a Hitachi TM4000 tabletop SEM in mixed mode with 15 kV.

1.4. Mechanical testing

Four (4) to five (5) samples in each material state were tensile tested in accordance with ASTM E8M – 16a on a Hounsfield uniaxial testing system using a strain rate of 0.16 mm/min. A round specimen with a gauge length of 25 mm and a minimum diameter of 4 mm was used. Four (4) to five (5) Charpy impact test specimens for each condition were produced by machining and wire-EDM according to ASTM E23-18. See Table 3 below which outlines the type of mechanical test performed, how many specimens were used for each material condition and which standard was used. Testing was conducted using standard v-shape notched specimens at room temperature and an impact velocity of 5.24 m/s.

1.5. Fatigue Testing

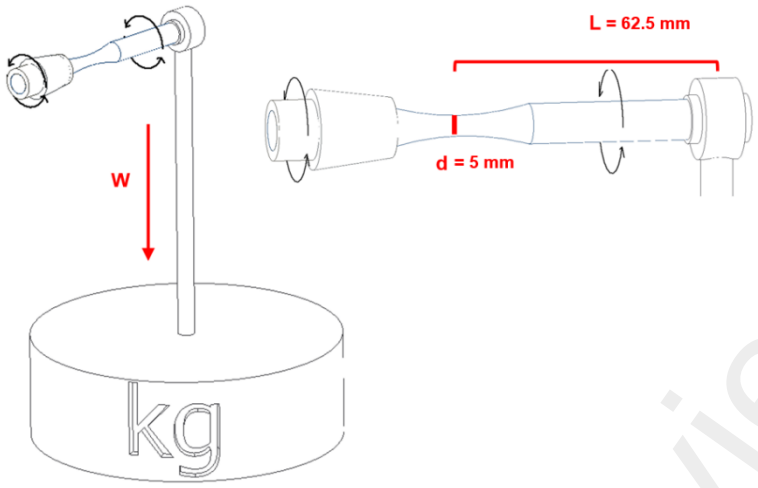

Figure 3: Rotating beam fatigue illustration.

15 round type fatigue specimens with a continuous radius between ends, in each material state, were machined using a lathe according to ASTM E466-15 as seen in Figure 3. The gauge sections were polished with an Ra < 0.2 µm in the longitudinal direction. Fatigue testing was conducted at UCD according to ASTM E466-15 using a Wohler-type cantilever rotating beam fatigue (RBF) system. Specimens were placed into chucks which were rotated using an electric motor at approximately 66Hz. Stress was induced by hanging a load at the other end of the specimen which was contained in a bearing as shown in Figure 3. The induced stress can be approximated as being fully reversed with a load ratio (R) of -1. Stress was calculated using equation 2.

$$Stress = 32WL/\pi d^3 \qquad Equation\ 2$$

Where *W* is the pplied Load, *L* is the Cantilever length and *d* is the minimum diamter in the specimen test section. The system had a resolution of 12.6 MPa / cycle. A cycle count of 10 million or more was recorded as a run out.

Table 3: Test procedure details

	Tensile test	Charpy impact test	Fatigue test
As-built (samples tested)	4	5	16
Heat-treated (samples tested)	5	5	17
HIP'ed (samples tested)	5	4	19
Wrought (samples tested)	5	5	15
Sample preparation	Lathe	Milled, wire EDM	Lathe, polished Ra < 0.2 µm
Test procedure	ASTM E8M – 16a	ASTM E23-18	ASTM E466-15 (rotating beam)
Specimen type	Specimen type 4	Standard 10x10x55 mm	Custom - following standard

2. Results and discussion

2.1. Microstructural Characterization

A detailed examination using SEM was carried out. Figure 4 presents a selection of the micrographs that highlight the findings. Figure 4 shows the as-built material possessed fine martensitic, needle like microstructure, with a lath thickness of 0.52 ± 0.09 µm, comparable to findings by Kaschel et. al [34, 35]. This type of microstructure is common in as-built Ti64 due to the high cooling rates experienced during the laser melting process [5, 35].

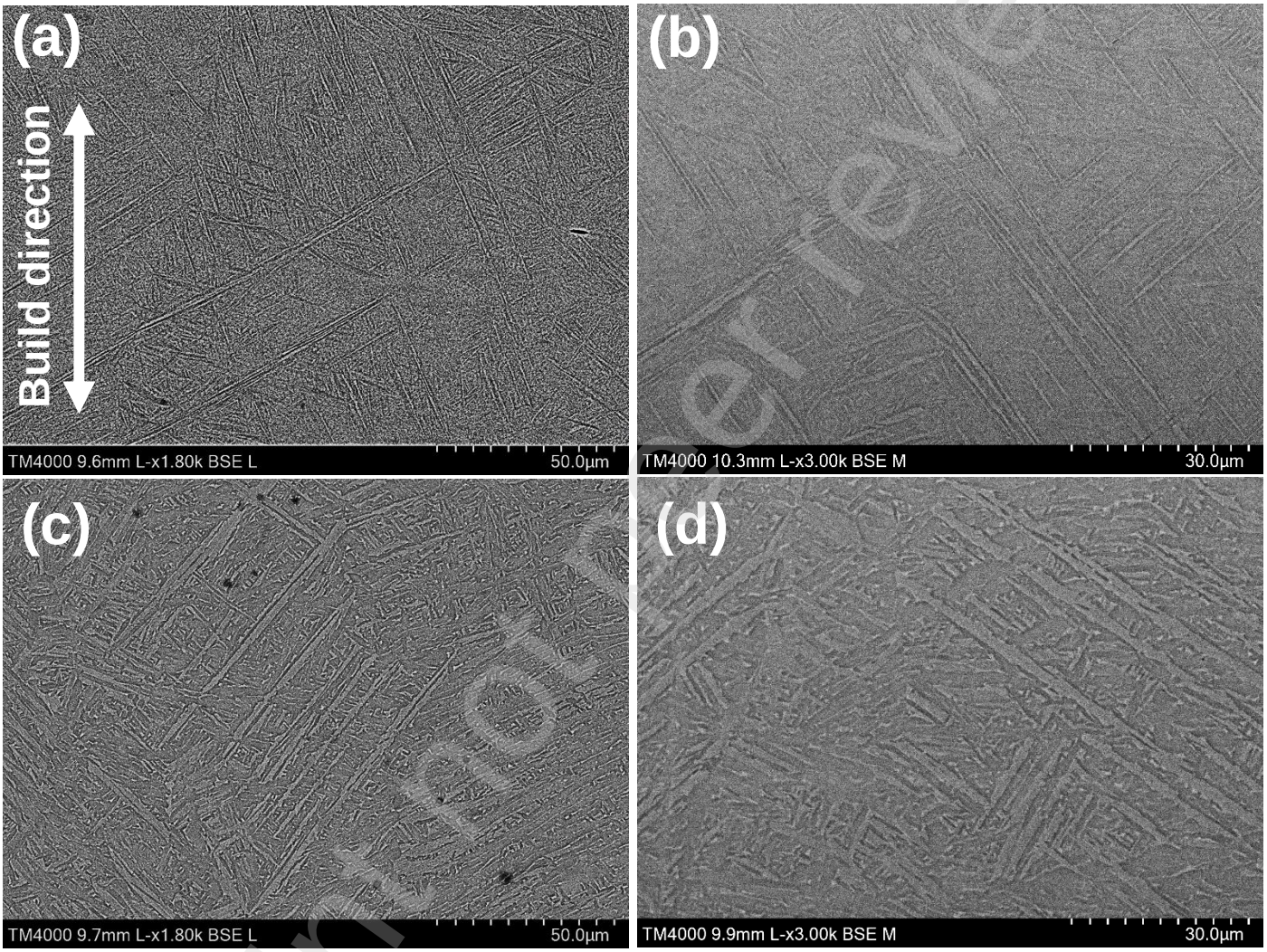

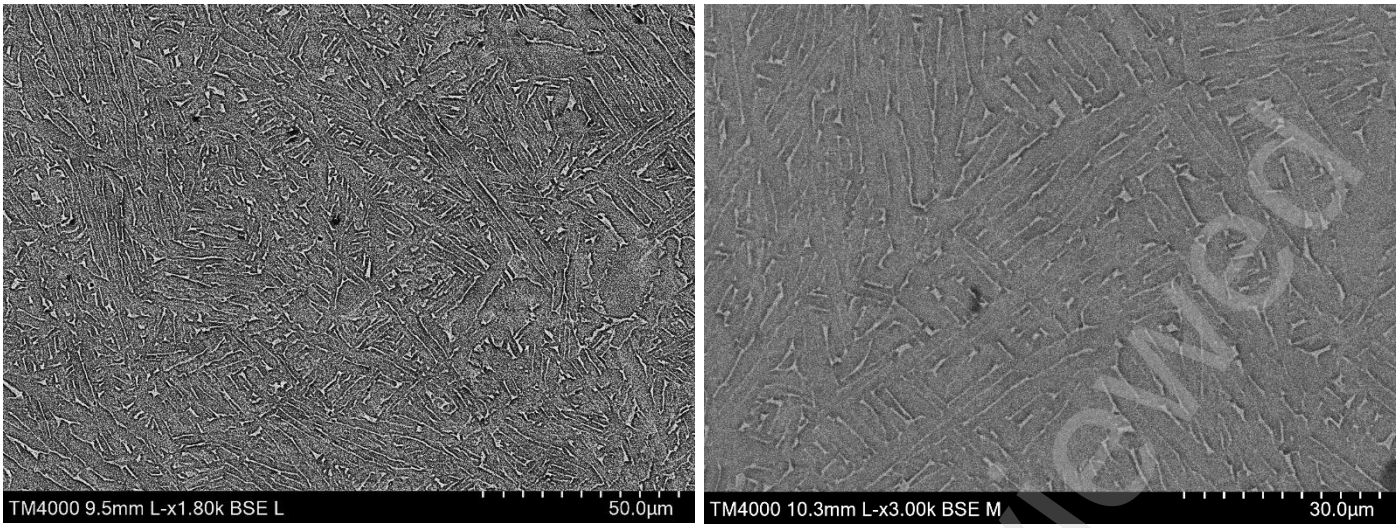

Figure 4: Microstructure analysis (a, b) as-built, (c, d) heat-treated, (e, f) HIP. The indicated build direction in (a) also applies to all other images.

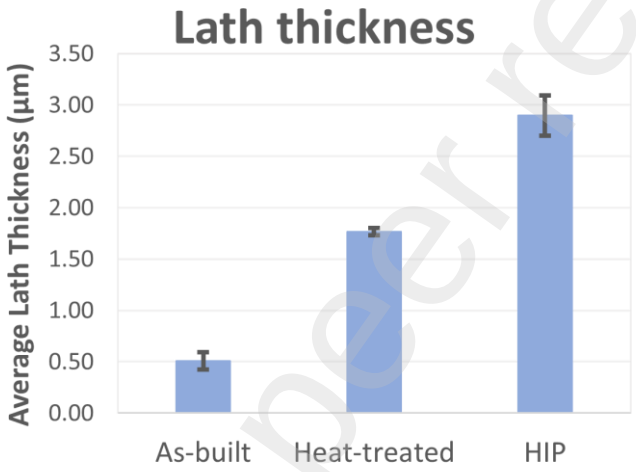

Figure 5: Lath thickness measurements

Coarsening of the phases with a lath thickness of 1.81 ± 0.04 µm is observed in the materials that were heat-treated. The α-lath thickness was measured and compared for as-built, heat-treated and HIP'ed material and the results are presented in Figure 5. The largest α-lath thickness was measured for the HIP'ed condition (2.90 ± 0.19 µm), similar to the values reported by Roudnicka [36] where the α-laths are fragmented when compared to heat-treated or the as-built condition. The examined conditions indicate dissimilar microstructures as shown by the differences in the α-lath thickness and morphology.

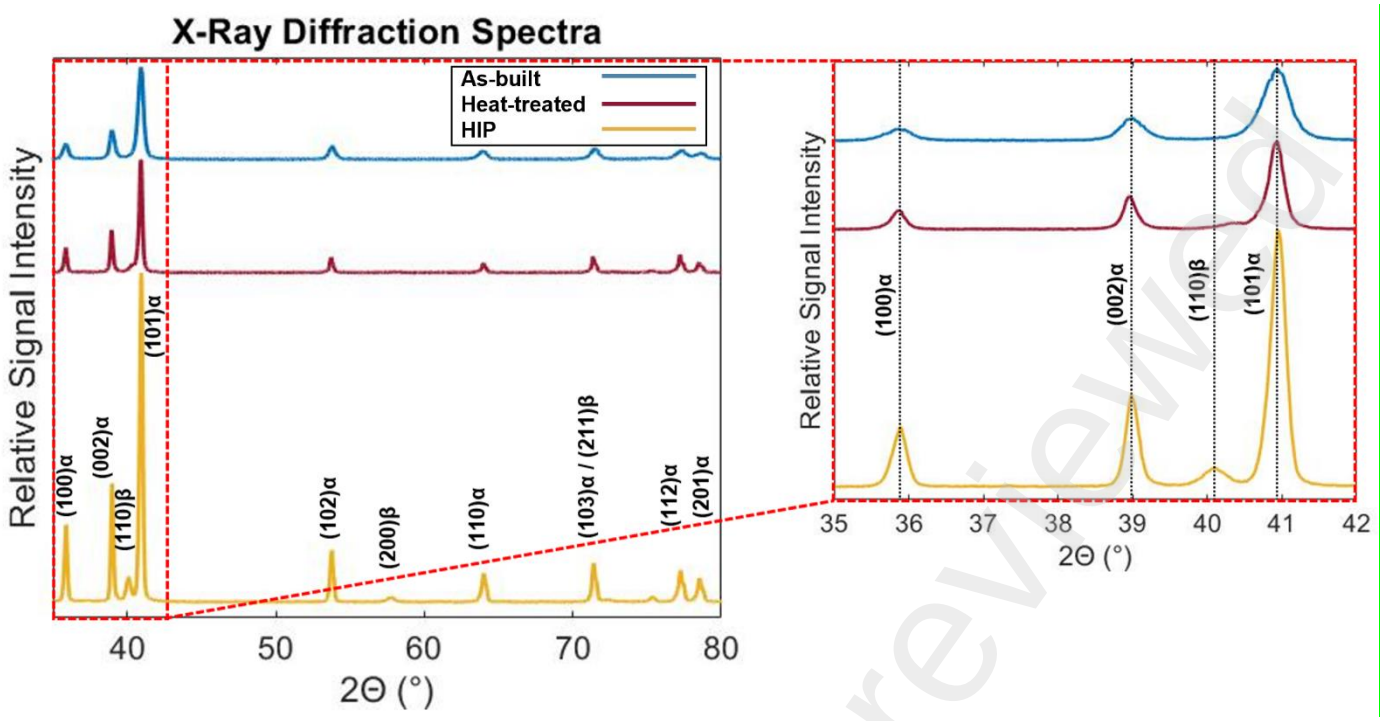

Figure 6: (left) XRD spectrum 2Θ range 35 - 80° with labeled peaks of interest, (right) XRD spectrum 2Θ range 35 - 42° with lines illustrating peak shift upon applying HIP

The XRD spectra presented in Figure 6, shows the comparison between as-built, heat-treated and HIP conditions. Peaks associated with the presence of *α*-phase (martensitic or equilibrium) are observed in all conditions. However, $(110)_{\beta}$ and $(200)_{\beta}$ peaks are only present in the heat-treated and HIP'ed material indicating activation of the phase transformation from $\alpha' \rightarrow (\alpha + \beta)_{eqm}$ upon HT or HIP. *B*-phase peaks are greater in relative intensity for the HIP'ed state when compared to the heat-treated condition. Therefore, it can be stated that higher amounts of *β*-phase were formed during HIP treatment than during heat-treatment. Closer examination of the 2Θ range 35 – 42° indicated that there is little to no peak shifting between the XRD spectra for as-built, heat-treated and HIP'ed materials.

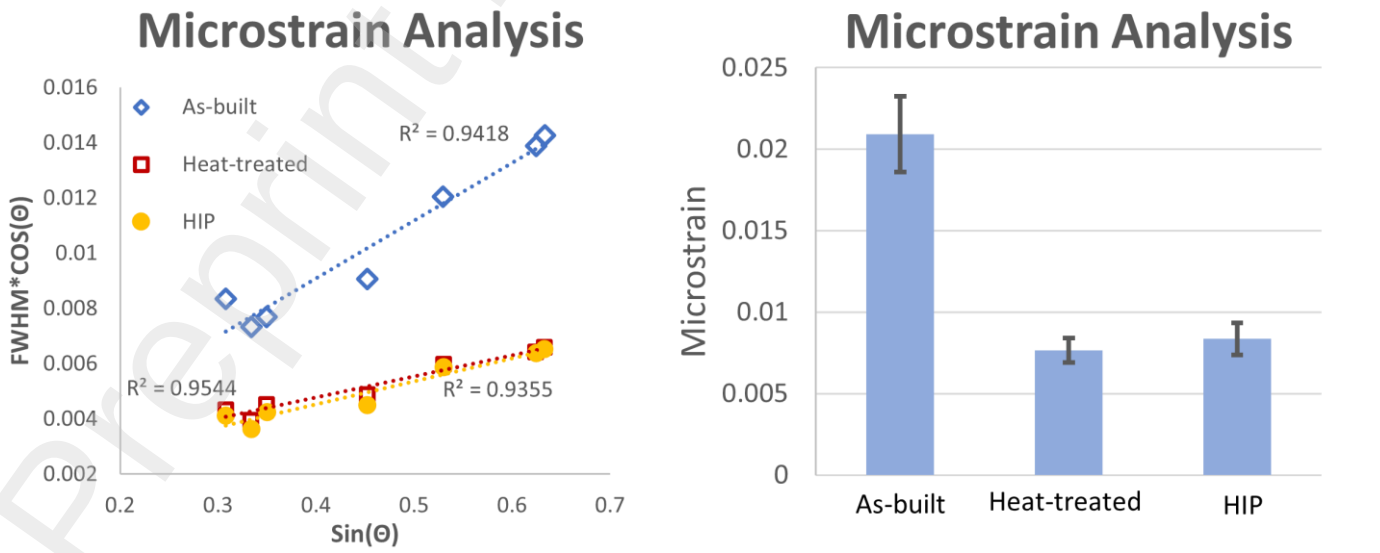

Figure 7: Microstrain analysis, plot to determine microstrain on the (left) and the resulting microsrain values (right)

Microstrain was determined using the Williamson-Hall method based on the XRD data (Figures 6) and is presented in Figure 7. Applying Equation 3 below, the full width half maxima (FWHM) was determined by curve fitting individual peaks using gaussian 1 type fits.

$$(FWHM) * cos(\theta) = k\lambda/(size) + (strain) * sin(\theta) \quad Equation\ 3$$

Where θ is the the angle between incident beam and the crystallographic reflecting plane, k is a peak shape factor and λ is the x-ray wavelength. Plotting $(FWHM) * cos(\theta)$ vs. $sin(\theta)$ as shown in Figure 7 (left) yields microstrain as the slope. The microstrain determined for the material measured as-built is found to be significantly higher than the microstrain determined for the heat-treated and HIP'ed materials. Heat-treatment and HIP had comparable microstrain indicating that both processes relieved residual and internal stresses to a similar degree.

2.2. MicroCT analysis

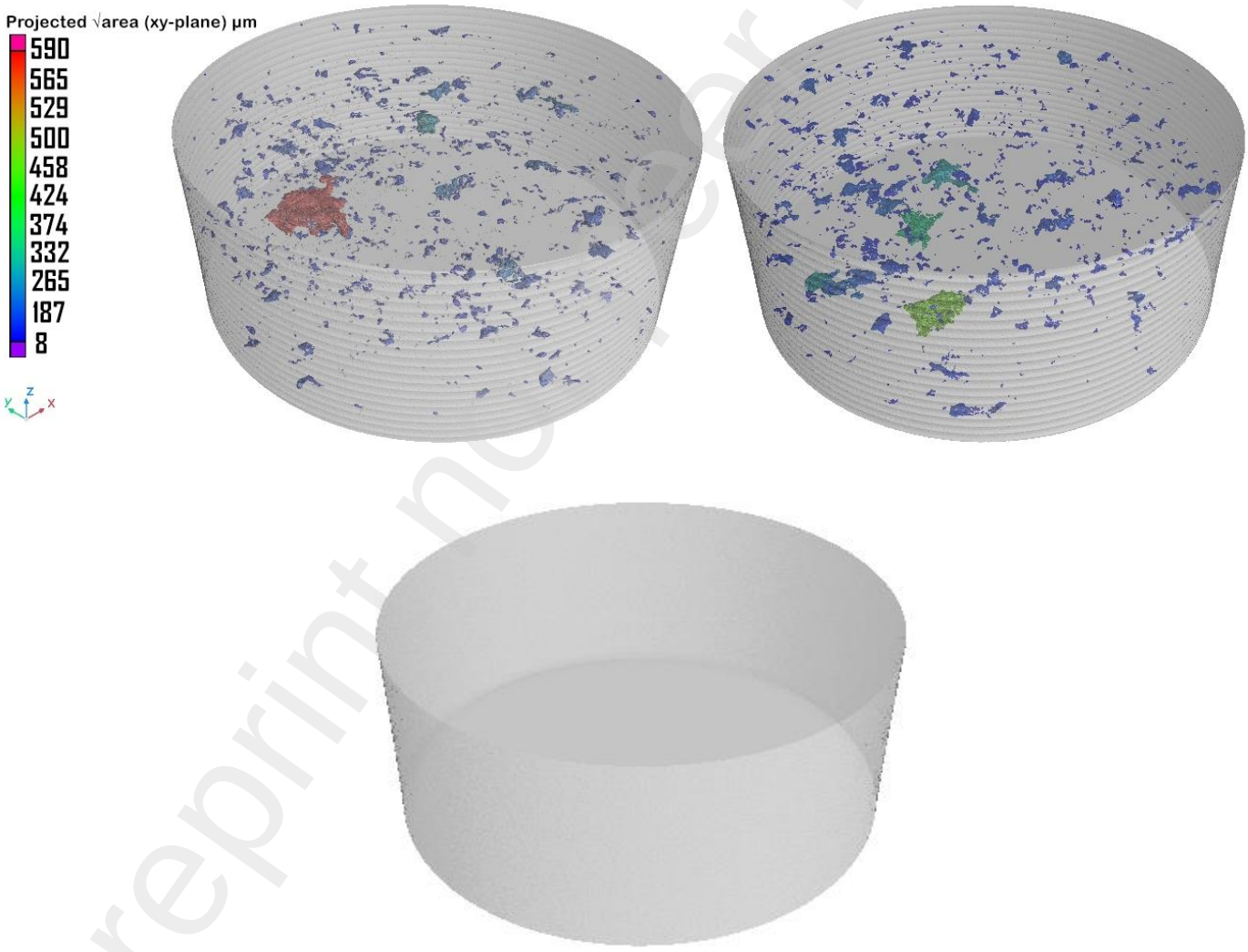

Figure 8: Transparent 3D depiction of the scanned microCT samples with a color scale bar indicating the square root of the projected void area in the x-y plane in µm. As-built (left), heat-treated (right) and HIP (bottom)

Figure 8 shows µCT scans of the gauge sections of as-built and heat-treated specimens. The regions scanned are in the center of the gauge section where fracture is most likely to occur during RBF testing.

Table 4: Porosity analysis

	Mean Porosity (%)	Mean $\sqrt{A}$ (µm)	D_{10} $\sqrt{A}$ (µm)	D_{50} $\sqrt{A}$ (µm)	D_{90} $\sqrt{A}$ (µm)
As-built	0.17 ± 0.10	28 ± 4	10 ± 2	18 ± 3	55 ± 7
Heat-treated	0.13 ± 0.08	28 ± 7	10 ± 1	17 ± 5	55 ± 14
HIP	0.00	0	0	0	0

µCT analysis was conducted on specimens that were then tested at 100 MPa, 200 MPa and 550 MPa, respectively. Quantitative examination of 7 scanned samples in each condition showed both the as-built and heat-treated conditions had similar levels of porosity which can be interpreted as an indication that heat-treatment does not affect porosity levels as expected.

2.3. Mechanical properties

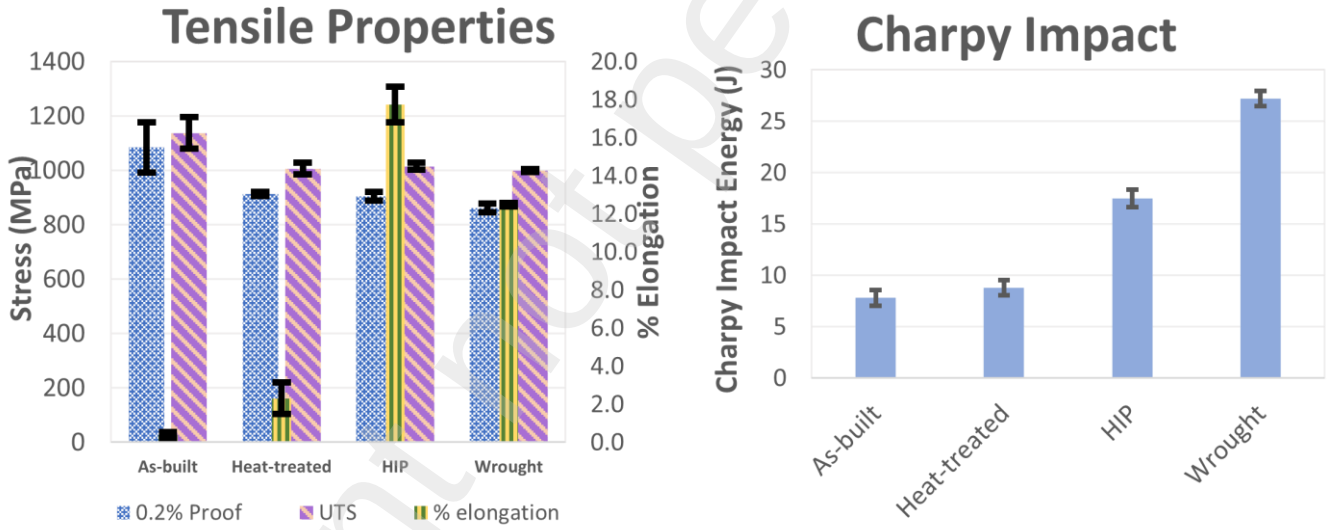

Figure 9: (left) tensile properties. The vertically striped bars correspond to the % elongation axis on the right, (right) Charpy impact values.

Tensile testing and Charpy impact test results of the as-built, heat-treated, HIP'ed and wrought material are summarized in Figure 9. The ultimate tensile strength (UTS) and the 0.2% proof yield stress values of the as-built material are higher than that of the heat-treated and HIP'ed material. This finding is consistent with the study conducted by Kasperovich et al. [37]. However, the % elongation values of the as-built and heat-treated samples (0.2% and 2.3%, respectively) was extremely low in comparison to the reported values in similar studies [11, 38]. This might indicate the use of non-optimal AM processing parameters for producing these parts, however since the

material was produced by a 3rd party the authors had no control over the process parameter selection. When material was HIP'ed, the ductility increased significantly to 17.8%. This is believed to be due to the removal of porosity during HIP. This theory is consistent with the results obtained using X-ray CT analysis. These are presented in Figure 8, which shows the representative CT models of the as-built, heat-treated and HIP'ed material. The differences in the tensile properties between as-built and heat-treated materials can be attributed to the microstructural coarsening leading to decreases in strength and an increase in ductility. Moreover, the formation of *β*-phase due to the activation of α' → $(\alpha + \beta)_{eqm}$ phase transformation is another factor that leads to the improved ductility and decreased strength. Lastly, microstrain in the as-built condition was determined to be higher than the heat-treated samples which can also be the reason for low ductility values found for as-built samples.

The results of the Charpy impact tests are shown in Figure 9, the as-built samples had the lowest impact toughness followed by the heat-treated, HIP'ed and wrought material. The x-ray CT data showed that there are similar porosity levels between these materials. HIP treatment significantly increased the impact toughness of the material significantly indicating that porosity is the controlling factor. Even though the focus of this study is understanding the effect of microstructural evolution upon post-processing of AM, wrought material has also been used as a reference in this study. The highest impact strength (27.2 joules) was determined for wrought Ti64 potentially due to the combined effects of finer microstructure, low porosity levels and residual stresses.

2.4. Fatigue life

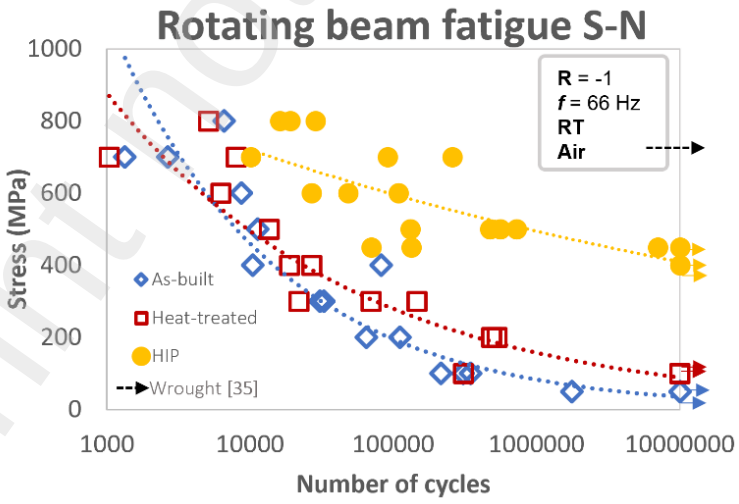

Figure 10: S-N curves generated by rotating beam fatigue testing.

Figure 10 above shows S-N curves obtained for the as-built, heat-treated and HIP'ed materials. Both the as-built and heat-treated exhibit relatively low fatigue strength when compared to the data presented in the literature. When optimal processing variables are used, fatigue endurance limits of

around 410 MPa - 550 MPa can be expected for L-PBF manufactured as-built / machined and stress relieved / machined Ti64 [5, 21, 29]. The present study estimates the endurance limit of the as-built material to be around 50 MPa and that of the heat-treated material to be around 100 MPa. This difference is possibly due to the higher than optimum levels of lack-of-fusion porosity formed during L-PBF. However, the main focus of this study is to understand the relative changes in fatigue limit between as-built and heat treated conditions where microstructure and residual stresses are the main variables.

Differences were observed between high cycle fatigue (HCF) and low cycle fatigue (LCF) behaviour in materials tested in the as-built and heat-treated conditions. At high fatigue stresses (LCF) >500 MPa, no significant difference was observed between as-built and heat-treated conditions. However, with the decrease in fatigue stresses, <500 MPa, a clear distinction between as-built and heat-treated materials was observed. The difference between high and low cycle fatigue behaviour in as-built and heat-treated conditions can be explained by the competing effects of porosity levels and microstructure / residual stress. On the other hand, material that was HIP'ed had both higher LCF and HCF strength than material tested in the as-built and heat-treated conditions indicating that the porosity level is the dominant controlling factor in fatigue deformation. However, when comparing samples with similar porosity levels (as-built and heat-treated) microstructural features along with residual stresses become critical in HCF i.e. the low stress regime. Process induced internal pores are the main factor in controlling fatigue and based on µCT-scans and fracture surface analysis (section 4.5), lack of fusion pores which are mainly present in this study (as-built and heat treated) form due to lower than optimum laser power and or excessive scan speeds [39]. This is supported by the fatigue strength of the HIP'ed material, around 400 MPa, which is significantly greater than the as-built and heat-treated conditions. Since HIP treatment has removed the porosity to a great extent, it is concluded that the presence of pores was the main contributing factor for the fatigue response of as-built and heat-treated samples. In addition to that, the as-built and heat-treated conditions still show differences in their fatigue response as the applied fatigue stress approaches the fatigue limit. The differences are not seen in the LCF but are pronounced in HCF regime. This is an indication that even though the presence of pores is the dominant factor in determining the fatigue limit of machined specimens, the microstructure as well as residual stresses influences specifically in the HCF regime.

Table 5: Fatigue mechanical and impact properties of tested materials

	Est. fatigue limit (MPa)	**UTS** (MPa)	**0.2% Proof stress** (MPa)	**% Elongation**	**Charpy impact energy** (J)
As-built	50	1138 ± 59	1084 ± 92	0.4 ± 0.2	7.8 ± 1
Heat-treated	100	1006 ± 21	914 ± 8	2.3 ± 0.8	9 ± 1
HIP	450	1015 ± 13	920 ± 15	17.8 ± 0.9	18 ± 1
Wrought	710 [24]	998 ± 6	862 ± 16	12.48 ± 0.1	27.2 ± 1

Table 5 summarises the numerical values of the estimated fatigue limit, UTS, 0.2% proof stress, % elongation and Charpy impact energy. The HCF response of the as-built, heat-treated and HIP'ed materials can be correlated with their ductility and Charpy impact energies, while no correlation between tensile strength and HCF response can be drawn. The low ductility determined in as-built and heat-treated materials has been attributed to the presence of large pores [40], which can be linked to the low fatigue limits of the material. Both the ductility and fatigue strength are severely reduced due to the increased stress concentration posed by large pores. On the other hand, increase in Charpy impact energy was obtained upon HIP treatment, where porosity levels decreased substantially along with microstructural coarsening. Previous study has shown that coarsened microstructure may also play a role in determining the impact energy in additively manufactured Ti64 [41]. Consistently, slight increase in impact energy values were obtained for heat-treated material when compared to the as-built. However, significant increase in the impact energy measurements of material that was HIP'ed is mainly due to removal of the pores. Therefore, defects and microstructure are both important factors in determining the overall fatigue strength in most commercial applications. Many other studies have found that non-HIP'ed AM material crack initiation sites are generally found at pores [10, 36–38], while in HIP'ed material the α-phase has been frequently identified as the crack initiator [28, 39, 40]. It can be stated that when a certain number of pores are present within the material the fatigue strength is predominantly influenced by these. Upon removal of these pores by HIP or (hypothetically) perfect optimization of an AM process, the microstructural features become one of the most influential factors along with residual stresses on the fatigue response.

2.5. Fracture surface analysis

The fracture surface in Figure 11 depicts as-built, heat-treated and HIP fatigue samples which had been stressed in HCF. The HCF is the region on the S-N curves where the greatest difference in fatigue response is seen. Therefore, these samples were selected for fracture surface analysis. In both as-built and heat-treated specimens, the origin of the initial crack could be traced back to relatively large lack of fusion porosity near the surface (Figure 11 b and d). On the other hand, in

the HIP'ed sample, the fracture surface analysis indicated that fatigue cracks initiated directly at the surface of the sample with no visible defects present (Figure 11 f).

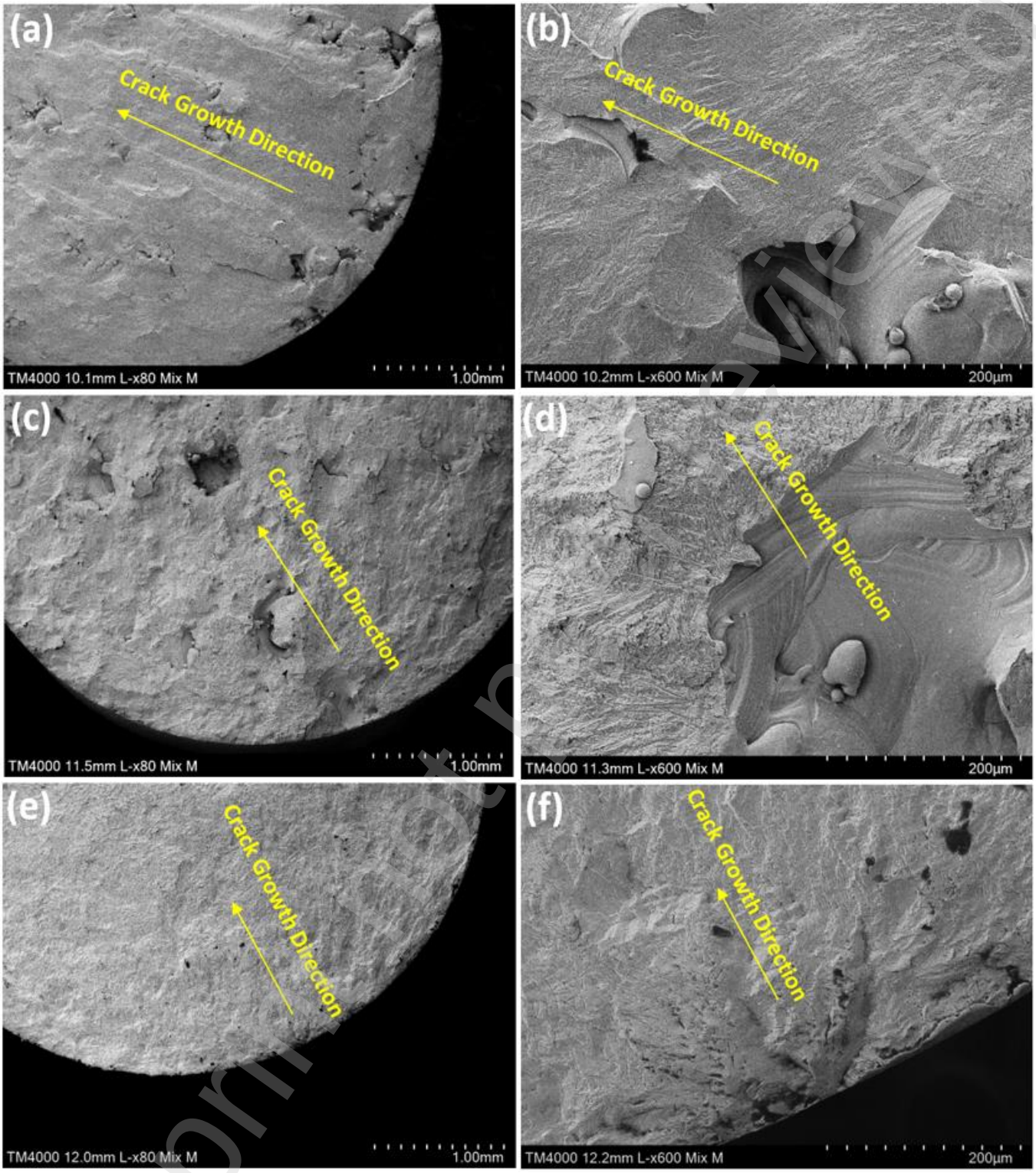

Figure 11: SEM images depict fatigue fracture surfaces imaged at 80X and 600X. (a, b) as-built sample stressed at 50 MPa which failed after 175,7920 cycles. (c, d) a heat-treated sample stressed at 200 MPa which failed after 48,3504 cycles (e, f) a HIP sample stressed at 450 MPa which failed after 70,037 cycles

In the HIP'ed material, there is evidence of stage I (shear mode) fatigue failure at the surface, where the fatigue cracks grew in a direction 45° normal to the loading direction. This was followed by stage II (tensile mode) in which the crack grew perpendicular to the loading direction (Figure 11 f).

Evidence of stage I is not observed on the fracture surfaces of the as-built and heat-treated specimens, examples of which are shown in Figure 11 a-d.

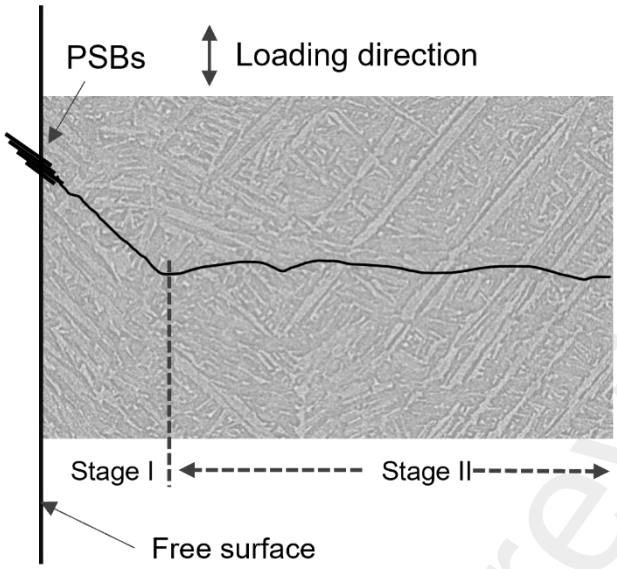

Figure 12: Schematic of stage I (shear mode), stage II (tensile mode)

Crack initiation in HIP occurred directly at the surface likely due to formation of persistent slip bands (PSBs) (Figure 12). In as-built and heat-treated conditions, crack initiation occurred at irregularly shaped pores near the surface. Such pores would cause an increase in the localized stress intensity which would mean cracks that first initiate at these pores are already progressed to a later stage of crack growth compared to HIP. From a fracture mechanics point of view, pores (voids) and cracks can both be considered discontinuities within the material. In the case where large irregularly shaped pores are present, the energy barrier for fatigue cracks to form is lower due to the highly localized stress intensity. Therefore, crack growth and early-stage crack growth become the deciding factor as to when final failure will occur. Similarly, the fatigue crack growth threshold stress intensity factor becomes critical in determining whether a fatigue load is high enough to cause a crack to propagate from a pore in the first place. The authors suggest that in the as-built and heat-treated conditions fatigue failure is dominated by crack growth, which has been shown to be sensitive to microstructure [42] and residual stresses [22]. This is consistent with the observed increase in fatigue limit upon heat-treatment, since coarser microstructure reduces the threshold stress intensity factor ΔK_{th} [22]. In the HIP'ed condition, on the other hand, fatigue is dominated by the crack initiation stage via the formation of slip bands on the surface of the material, which has been shown to be probabilistic in nature [43]. On the other hand, the difference between the fatigue strength of the HIP'ed and wrought conditions may be due to the vastly different microstructures. The wrought equiaxed microstructure is more resistant to crack initiation than the lamellar α + β microstructure of the material in the HIP'ed condition.

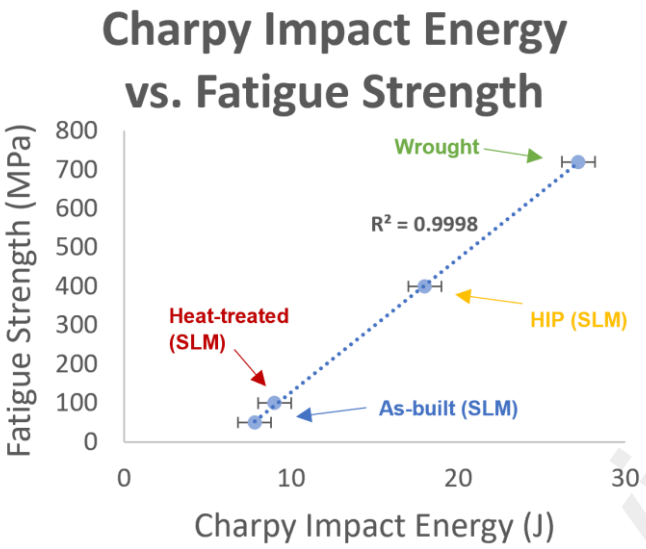

Figure 13: Charpy impact fatigue strength relation

A direct linear correlation is found between Charpy impact toughness and fatigue strength for all conditions examined in this study (Figure 13). Similarly, in a study by Soundarapandiyan et al. the application of HIP treatment to as-built EBM material increased not only the fatigue life from 10^5 cycles to 10^7 at 600 MPa, but also the Charpy impact energy from 47 to 71 J [44]. Increase in the Charpy impact energy upon HIP in EBM Ti64 has also been reported by W.A. Grell et al. and an inverse relationship between Charpy impact energy and oxygen content was also shown [45]. Martínez et al. have shown Charpy impact energy together with tensile and hardness testing can be used to predict the fatigue life of high strength steels [46].

The as-built and heat-treated fatigue response has been shown to be dominated by the presence of porosity, while the fatigue deformation of HIP'ed AM material is found to be more microstructurally controlled. However, in both cases the linear correlation between Charpy impact energy and fatigue strength persists. This result is significant as it might be used as a tool to predict fatigue limit in a cost-effective way for AM Ti64 alloy. A possible explanation for this correlation may be that; although different failure mechanisms are at play between fatigue and impact testing, both are controlled by the same structural features, such as microstructure, porosity level and phase content. Slight increase in fatigue strength and Charpy impact energy upon heat-treatment is possibly due to the phase transformation α' → α+β, coarsening of the laths and the resulting increase in ductility. The significant increase in fatigue strength and Charpy impact energy upon HIP can be attributed to the same factors with the addition of the drastic reduction in porosity levels. However, further investigation is needed in order to understand the links between controlling fatigue mechanisms in LPBF Ti64 under different conditions and impact energy. This will shed-light into the development of more fatigue resistant AM Ti-based alloys which can widen the use of AM technology both in biomedical and aerospace industries.

Conclusion

- Post-processing of AM Ti64 alloys via Heat treatment or HIP significantly altered the as-built microstructure by coarsening the α-laths and reduced micro-strain. It was also determined that phase transformation α' → α+β is activated for both conditions. Upon heat treatment no change in the size or percentage of pores was observed, whereas significant reduction in porosity level upon application of HIP is clear.
- The difference in HCF response between heat-treated vs. as-built conditions shows that factors other than porosity levels can influence fatigue life, even when extremely large pores are present. This difference in fatigue response is attributed to the coarsening of the microstructure, activation of phase transformation ($\alpha' \rightarrow (\alpha + \beta)_{eqm}$) upon heat treatment and the decrease in microstrain. These microstructural changes are also reflected in the increase in ductility from 0.4% to 2.3% via the heat treatment.
- Fractography analysis indicates that fatigue cracks which lead to failure in as-built and heat-treated samples initiated at large lack-of-fusion porosity which were positioned close to the surface, while in HIP samples cracks originate from the surface with no visible defects present.
- A higher degree of scattering is observed in HIP fatigue data when compared to as-built and heat-treated. This may be an indication that HIP failure is more probabilistic in nature, likely because it is more dependent on crack initiation via the formation of slip bands, while in as-built and heat-treated samples the fatigue is controlled by crack growth due to the presence of easy crack initiation sites such as lack-of-fusion pores prior to fatigue.
- A strong linear relationship between the impact energy and fatigue limit was determined which should be further investigated as this correlation can be used as a modelling tool to predict fatigue limit for AM Ti64 alloy.

Credit authorship contribution statement

Bryan Naab: Investigation, Writing-Original Draft

Mert Celikin: Writing - Review & Editing, Supervision

Originality statement

I write on behalf of myself and all co-authors to confirm that the results reported in the manuscript are original and neither the entire work, nor any of its parts have been previously published. The authors confirm that the article has not been submitted to peer review, nor has been accepted for publishing in another journal. The author(s) confirms that the research in their work is original, and that all the data given in the article are real and authentic. If necessary, the article can be recalled, and errors corrected.

Funding

This research was co-funded by the Science Foundation Ireland (SFI) and Stryker through I-Form, the SFI Research Centre for Advanced Manufacturing and the Advanced Metallic Systems Centre for Doctorial Training (AMS – CDT).

Acknowledgements

This publication has emanated from research conducted with the financial support of Science Foundation Ireland under Grant number 16/RC/3872. For the purpose of Open Access, the author has applied a CC BY public copyright license to any Author Accepted Manuscript version arising from this submission.

Data availability statement

The data that support the findings of this study are available from the corresponding author, B. N., upon reasonable request.

References

1. Milewski JO (2017) Current System Configurations. In: Milewski JO (ed) Additive Manufacturing of Metals: From Fundamental Technology to Rocket Nozzles, Medical Implants, and Custom Jewelry. Springer International Publishing, Cham, pp 131–179

2. D. Bourell, H. Kuhn, W. Frazier, M. Seifi, editors (2020) Additive Manufacturing of Titanium Alloys. In: ASM Handbook, Volume 24, Additive Manufacturing Processes

3. Edwards P, Ramulu M (2014) Fatigue performance evaluation of selective laser melted Ti–6Al–4V. Materials Science and Engineering: A 598:327–337. https://doi.org/10.1016/j.msea.2014.01.041

4. Zhao X, Li S, Zhang M, et al (2016) Comparison of the microstructures and mechanical properties of Ti–6Al–4V fabricated by selective laser melting and electron beam melting. Materials & Design 95:21–31. https://doi.org/10.1016/j.matdes.2015.12.135

5. Qian M, Xu W, Brandt M, Tang HP (2016) Additive manufacturing and postprocessing of Ti-6Al-4V for superior mechanical properties. MRS Bulletin 41:775–784. https://doi.org/10.1557/mrs.2016.215

6. Edwards P, O'Conner A, Ramulu M (2013) Electron Beam Additive Manufacturing of Titanium Components: Properties and Performance. Journal of Manufacturing Science and Engineering 135:061016. https://doi.org/10.1115/1.4025773

7. Cunningham R, Narra SP, Ozturk T, et al (2016) Evaluating the Effect of Processing Parameters on Porosity in Electron Beam Melted Ti-6Al-4V via Synchrotron X-ray Microtomography. JOM 68:765–771. https://doi.org/10.1007/s11837-015-1802-0

8. Zhang M, Sun C-N, Zhang X, et al (2017) Fatigue and fracture behaviour of laser powder bed fusion stainless steel 316L: Influence of processing parameters. Materials Science and Engineering: A 703:251–261. https://doi.org/10.1016/j.msea.2017.07.071

9. Tammas-Williams S, Withers PJ, Todd I, Prangnell PB (2016) The Effectiveness of Hot Isostatic Pressing for Closing Porosity in Titanium Parts Manufactured by Selective Electron Beam Melting. Metall and Mat Trans A 47:1939–1946. https://doi.org/10.1007/s11661-016-3429-3

10. Tammas-Williams S, Withers PJ, Todd I, Prangnell PB (2017) The Influence of Porosity on Fatigue Crack Initiation in Additively Manufactured Titanium Components. Sci Rep 7:7308. https://doi.org/10.1038/s41598-017-06504-5

11. Kasperovich G, Hausmann J (2015) Improvement of fatigue resistance and ductility of TiAl6V4 processed by selective laser melting. Journal of Materials Processing Technology 220:202–214. https://doi.org/10.1016/j.jmatprotec.2015.01.025

12. Qiu C, Adkins NJE, Attallah MM (2013) Microstructure and tensile properties of selectively laser-melted and of HIPed laser-melted Ti–6Al–4V. Materials Science and Engineering: A 578:230–239. https://doi.org/10.1016/j.msea.2013.04.099

13. Jamshidi P, Aristizabal M, Link to external site this link will open in a new window, et al (2020) Selective Laser Melting of Ti-6Al-4V: The Impact of Post-processing on the Tensile, Fatigue and Biological Properties for Medical Implant Applications. Materials 13:2813. http://dx.doi.org/10.3390/ma13122813

14. Yingliu A (2017) Quintus Hot Isostatic Presses with URC^{TM}. http://quintustechnologies.com/app/uploads/2017/04/reference-sheet-anhui-a4.pdf. Accessed 25 Aug 2022

15. Liu S, Shin YC (2019) Additive manufacturing of Ti6Al4V alloy: A review. Materials and Design 164:23. https://doi.org/10.1016/j.matdes.2018.107552

16. Kasperovich G, Haubrich J, Gussone J, Requena G (2016) Correlation between porosity and processing parameters in TiAl6V4 produced by selective laser melting. Materials & Design 105:160–170. https://doi.org/10.1016/j.matdes.2016.05.070

17. Viet-Duc L, Etienne P, Franck M, François E (2018) Influence of porosity on the fatigue behaviour of additively fabricated TA6V alloys. In: MATEC Web of Conferences, Fatigue 2018. p 9

18. Stef J, Poulon-Quintin A, Redjaimia A, et al (2018) Mechanism of porosity formation and influence on mechanical properties in selective laser melting of Ti-6Al-4V parts. Materials & Design 156:480–493. https://doi.org/10.1016/j.matdes.2018.06.049

19. Liu W, Chen C, Shuai S, et al (2020) Study of pore defect and mechanical properties in selective laser melted Ti6Al4V alloy based on X-ray computed tomography. Materials Science and Engineering: A 797:139981. https://doi.org/10.1016/j.msea.2020.139981

20. Vayssette B, Saintier N, Brugger C, et al (2018) Surface roughness of Ti-6Al-4V parts obtained by SLM and EBM: Effect on the High Cycle Fatigue life. Procedia Engineering 213:89–97. https://doi.org/10.1016/j.proeng.2018.02.010

21. Rafi HK, Karthik NV, Gong H, et al (2013) Microstructures and Mechanical Properties of Ti6Al4V Parts Fabricated by Selective Laser Melting and Electron Beam Melting. J of Materi Eng and Perform 22:3872–3883. https://doi.org/10.1007/s11665-013-0658-0

22. Leuders S (2013) On the mechanical behaviour of titanium alloy TiAl6V4 manufactured by selective laser melting: Fatigue resistance and crack growth performance. International Journal of Fatigue 8

23. Mower TM, Long MJ (2016) Mechanical behavior of additive manufactured, powder-bed laser-fused materials. Materials Science and Engineering: A 651:198–213. https://doi.org/10.1016/j.msea.2015.10.068

24. ASM Handbook (1996) Fatigue and Fracture

25. Leyens C, Peters M (2003) Titanium and Titanium Alloys: Fundamentals and Applications, 1st ed. Wiley

26. Nakatani M, Masuo H, Tanaka Y, Murakami Y (2019) Effect of Surface Roughness on Fatigue Strength of Ti-6Al-4V Alloy Manufactured by Additive Manufacturing. Procedia Structural Integrity 19:294–301. https://doi.org/10.1016/j.prostr.2019.12.032

27. Naab B, Dowling DP, Celikin M (2022) The Study on Microstructural Evolution During Post-processing of Additively Manufactured Ti64. In: TMS 2022 151st Annual Meeting & Exhibition Supplemental Proceedings. Springer International Publishing, Cham, pp 198–207

28. Kaschel FR, Vijayaraghavan RK, Shmeliov A, et al (2020) Mechanism of stress relaxation and phase transformation in additively manufactured Ti-6Al-4V via in situ high temperature XRD

and TEM analyses. Acta Materialia 188:720–732. https://doi.org/10.1016/j.actamat.2020.02.056

29. Wycisk E (2014) Effects of Defects in Laser Additive Manufactured Ti-6Al-4V on Fatigue Properties. Physics Procedia 8

30. Gerrit Ter Haar, Thorsten Becker (2018) Selective Laser Melting Produced Ti-6Al-4V: Post-Process Heat Treatments to Achieve Superior Tensile Properties. Materials 11:146. https://doi.org/10.3390/ma11010146

31. Wang D, Dou W, Yang Y (2018) Research on Selective Laser Melting of Ti6Al4V: Surface Morphologies, Optimized Processing Zone, and Ductility Improvement Mechanism. Metals 8:471. https://doi.org/10.3390/met8070471

32. Vrancken B, Thijs L, Kruth J-P, Van Humbeeck J (2012) Heat treatment of Ti6Al4V produced by Selective Laser Melting: Microstructure and mechanical properties. Journal of Alloys and Compounds 541:177–185. https://doi.org/10.1016/j.jallcom.2012.07.022

33. Khorsand Zak A, Abd. Majid WH, Abrishami ME, Yousefi R (2011) X-ray analysis of ZnO nanoparticles by Williamson–Hall and size–strain plot methods. Solid State Sciences 13:251–256. https://doi.org/10.1016/j.solidstatesciences.2010.11.024

34. Zhai Y, Galarraga H, Lados DA (2016) Microstructure, static properties, and fatigue crack growth mechanisms in Ti-6Al-4V fabricated by additive manufacturing: LENS and EBM. Engineering Failure Analysis 69:3–14. https://doi.org/10.1016/j.engfailanal.2016.05.036

35. R. Kaschel F, Celikin M, Dowling DP (2020) Effects of laser power on geometry, microstructure and mechanical properties of printed Ti-6Al-4V parts. Journal of Materials Processing Technology 278:116539. https://doi.org/10.1016/j.jmatprotec.2019.116539

36. Roudnicka M, Mertova K, Vojtech D (2019) Influence of hot isostatic pressing on mechanical response of as-built SLM titanium alloy. IOP Conf Ser: Mater Sci Eng 629:012034. https://doi.org/10.1088/1757-899X/629/1/012034

37. Kasperovich G, Hausmann J (2015) Improvement of fatigue resistance and ductility of TiAl6V4 processed by selective laser melting. Journal of Materials Processing Technology 220:202–214. https://doi.org/10.1016/j.jmatprotec.2015.01.025

38. Cain V, Thijs L, Van Humbeeck J, et al (2015) Crack propagation and fracture toughness of Ti6Al4V alloy produced by selective laser melting. Additive Manufacturing 5:68–76. https://doi.org/10.1016/j.addma.2014.12.006

39. Bai Q, Wu B, Qiu X, et al (2020) Experimental study on additive/subtractive hybrid manufacturing of 6511 steel: process optimization and machining characteristics. The International Journal of Advanced Manufacturing Technology 108:1–10. https://doi.org/10.1007/s00170-020-05514-4

40. Kumar P, Ravi Chandran KS, Cao F, et al (2016) The Nature of Tensile Ductility as Controlled by Extreme-Sized Pores in Powder Metallurgy Ti-6Al-4V Alloy. Metall Mater Trans A 47:2150–2161. https://doi.org/10.1007/s11661-016-3419-5

41. Hrabe N, White R, Lucon E (2019) Effects of internal porosity and crystallographic texture on Charpy absorbed energy of electron beam melting titanium alloy (Ti-6Al-4V). Materials Science and Engineering: A 742:269–277. https://doi.org/10.1016/j.msea.2018.11.005

42. Galarraga H, Warren RJ, Lados DA, et al (2017) Fatigue crack growth mechanisms at the microstructure scale in as-fabricated and heat treated Ti-6Al-4V ELI manufactured by electron beam melting (EBM). Engineering Fracture Mechanics 176:263–280. https://doi.org/10.1016/j.engfracmech.2017.03.024

43. Jha SK, Larsen JM, Rosenberger AH (2009) Towards a physics-based description of fatigue variability behavior in probabilistic life-prediction. Engineering Fracture Mechanics 76:681–694. https://doi.org/10.1016/j.engfracmech.2008.10.013

44. Soundarapandiyan G, Khan R, Johnston C, et al (2021) Effect of postprocessing thermal treatments on electron-beam powder bed–fused Ti6Al4V. Material Design & Processing Communications 3:e168. https://doi.org/10.1002/mdp2.168

45. Grell WA, Solis-Ramos E, Clark E, et al (2017) Effect of powder oxidation on the impact toughness of electron beam melting Ti-6Al-4V. Additive Manufacturing 17:123–134. https://doi.org/10.1016/j.addma.2017.08.002

46. Martínez A, Jaimes A, Serna A, Uribe I (2010) Development of a correlation to estimate the fatigue strength for steels based on low-cost tests. CT&F - Ciencia, Tecnología y Futuro 4:13